The impact of chromium coatings on Zircaloy cladding deformation behavior under reactivity-initiated accident–like mechanical loading conditions

Jennifer I. Espersen[a], Ben E. Garrison[b], Kory Linton[b], Koroush Shirvan[c], Nathan A. Capps[b], Nicholas R. Brown[a]

[a] Department of Nuclear Engineering, University of Tennessee, Knoxville, TN, USA

[b] Oak Ridge National Laboratory, Oak Ridge, TN, USA

[c] Massachusetts Institute of Technology, Cambridge, MA, USA

Keywords: reactivity-initiated accident, modified burst test, cladding, coated Zircaloy, accident-tolerant fuel

Highlights

- Modified burst testing was used to experimentally simulate the mechanical response of nuclear fuel cladding subjected to reactivity-initiated accident–like mechanical test conditions.
- Uncoated Zircaloy-4 and chromium-coated Zircaloy-4 specimens were tested using the modified burst test, and in situ strain data was obtained using digital image correlation analysis.
- Chromium-coated Zircaloy-4 samples were found to burst at lower hoop strains than the uncoated Zircaloy-4 control group samples.

Abstract

A reactivity-initiated accident (RIA) is the result of a control rod ejection or control blade drop, causing an increase in the fission rate. The resulting injection of energy causes rapid thermal expansion of the fuel pellet due to the rapid increase in temperatures. This thermal expansion may result in pellet–cladding mechanical interaction (PCMI), whereby the fuel imparts a mechanical strain to the cladding. PCMI may cause the cladding to fail, and thus the mechanical response of cladding due to PCMI must be investigated when characterizing new cladding materials. Chromium-coated Zircaloy-4 is a near-term accident-tolerant fuel cladding that exhibits improved high-temperature oxidation resistance. In this work, modified burst testing was utilized to experimentally simulate the effects of PCMI on both uncoated and chromium-coated Zircaloy cladding samples at hot zero power conditions. Samples were coated using either cold-spraying or physical vapor deposition (PVD) to understand the differences in behavior that the coating application method may cause. Digital image correlation was used to analyze images of the deforming specimens to extract the cladding's in situ strain behavior. The uncoated specimens

This manuscript has been authored by UT-Battelle, LLC under contract DE-AC05-00OR22725 with the US Department of Energy (DOE). The US government retains and the publisher, by accepting the article for publication, acknowledges that the US government retains a nonexclusive, paid-up, irrevocable, worldwide license to publish or reproduce the published form of this manuscript, or allow others to do so, for US government purposes. DOE will provide public access to these results of federally sponsored research in accordance with the DOE Public Access Plan (http://energy.gov/downloads/doe-public-access-plan).

were shown to burst at hoop strains ranging from 8.8% to 17.2%. The cold-sprayed chromium-coated Zircaloy specimens burst at hoop strains of 7.0% to 11.0%. The PVD-coated tubes burst at hoop strains of 9.1% to 11.5%. These results indicate that the chromium coating causes a loss of ductility in the cladding. The higher burst hoop strains of the PVD-coated samples relative to the cold-sprayed samples indicate that the cold spraying technique causes a greater loss of ductility than the PVD method.

1. Introduction

The nuclear industry is working to enhance the accident tolerance of Zircaloy, a zirconium-based alloy [1]. Accident-tolerant fuel (ATF) systems [1–13] are fuel and cladding systems for light-water reactors (LWRs) that exhibit an improved safety response to accident conditions while maintaining or improving upon the good operational characteristics of current fuel and cladding systems (UO_2 and Zircaloy). ATF cladding should have favorable characteristics for normal operation (low neutron absorption cross-section, high melting point, radiation resistance, oxidation and corrosion resistance at operating temperatures, and minimal interactions with water) as well as high-temperature oxidation resistance, minimal hydrogen generation, and good dimensional stability [3,14]. Additionally, ATF cladding materials should be able to cope with accident conditions better than Zircaloy [3]. One such accident scenario is the reactivity-initiated accident (RIA), during which pellet–cladding mechanical interaction (PCMI) may cause cladding rupture. To mitigate this, cladding materials should be designed to maintain good ductility [3]. The second motivation for improved cladding materials is to support higher burnups of nuclear fuel and large-scale power uprates. The nuclear industry aims to extend the cycle length of LWRs, which would increase burnup levels beyond the current peak rod average burnup of 62 GWd/tU [15]. However, at higher burnups, Zircaloy cladding loses its ductility due to radiation-induced damage, and hydrogen embrittlement occurs from hydrogen uptake as the waterside corrodes [16]. In addition, large-scale power uprates in conjunction with higher burnups will result in the fuel being operated at higher powers for longer periods of time. Therefore, to meet the goals of both ATFs and high burnup, an oxidation-resistant cladding with good ductility is needed.

A near-term cladding candidate is chromium-coated Zircaloy [17,18]. Zircaloy exhibits desirable qualities for normal operation, and the chromium coating protects the waterside surface of the cladding from oxidation and hydride pickup. While Zircaloy exhibits good ductility on its own, the effects of the added coating on its deformation behavior must be investigated. In the work documented herein, the deformation behavior of chromium-coated Zircaloy cladding under RIA-like conditions was investigated using a modified burst test (MBT) [19]. Several experiments were performed on uncoated Zircaloy-4 and chromium-coated Zircaloy-4. For the coated tests, two different coating methods were explored: cold spray and physical vapor deposition (PVD) [20].

RIAs are caused by a control rod ejection in pressurized water reactors (PWRs) or a control rod drop in boiling water reactors (BWRs), and they result in a rapid increase in the fission rate in a localized area of the fuel [21]. This higher fission rate causes the fuel temperature to increase

swiftly, resulting in thermal expansion. As it expands, the fuel may impart a mechanical strain to the cladding, especially if the fuel–cladding gap has already closed. This is the low-temperature phase of a RIA, and this phase is the focus of the present study. The low-temperature phase of a RIA may last for tens of milliseconds to hundreds of milliseconds, and a high enough strain rate may cause the cladding to burst [22].

To experimentally simulate the PCMI during a RIA, MBTs were developed at Oak Ridge National Laboratory [19,23] based on a design by the Electric Power Research Institute [24,25]. Discussed in greater depth in the Methods section, the MBT setup offers the capability of varying the pulse width of the transient, which makes it possible to better understand the mechanical behavior of cladding under a variety of rapid loading conditions. Additionally, the setup uses digital image correlation (DIC) analysis to calculate the in situ strain of specimens across the entire surface of the cladding. MBT is a separate-effects testing rig designed to investigate the mechanical deformation behavior of nuclear fuel cladding under RIA-like conditions due to PCMI at hot zero power (HZP), room temperature, or in between. Multiple studies have utilized MBTs in the past to analyze a variety of materials, including ZIRLO, iron-chromium-aluminum (FeCrAl) alloy tubes, and silicon carbide (SiC) fiber-reinforced/SiC matrix (SiC/SiC) composite tubes [19,22,26].

2. Methods

2.1 Materials

Unirradiated Zircaloy-4 cladding was utilized for this study. The uncoated Zircaloy-4 tubes had an outer diameter of 9.5 mm and a wall thickness of 0.56 mm. See Table 1 for the chemical composition of the specimens. Some tests were performed on uncoated Zircaloy-4; these tests served as a control group to better understand how the coating affects the strain behavior of the cladding. For the coated cladding specimens, some were cold spray-coated, while others were PVD-coated. This configuration allowed for an understanding of whether one coating method is more desirable than the other. All coated specimens were coated with pure chromium.

Table 1. Chemical composition of Zircaloy-4 cladding specimens [27].

Element	**Zr**	**Sn**	**Fe**	**O**	**Cr**
Weight (%)	98.23	1.32	0.21	0.13	0.11

The cold spray methods used in this work are discussed in greater depth in Hazan et al. [27], but key details are discussed here. The cold spray system operated with helium as a carrier at a flow rate of around 1300 m^3/hr, a pressure of 3.1 MPa, and a temperature of 675 °C. The tungsten carbide nozzle was positioned 2.5 cm from the cladding specimens and had a gun speed of 200 mm/s.

Cladding specimens were 25.4 mm long and were attached to a driver tube with Aremco 671 ceramic adhesive and allowed to cure for at least 24 hours before experimentation [28]. The driver tube was made of age-hardened Inconel 718 and had a thin-walled region surrounded by thick-walled regions (see Figure 1). The thin- and thick-walled regions were 0.45 and 0.98 mm thick, respectively. The cladding specimens were coated with engine-grade paint: first a complete coat of white followed by a sparse spraying of black to provide a speckle pattern (see Figure 2) for analysis via the DIC software, discussed further in the DIC Analysis section. Tests were set up and run quickly after the paint was applied to prevent it from curing and flaking off the surface of the specimen during deformation.

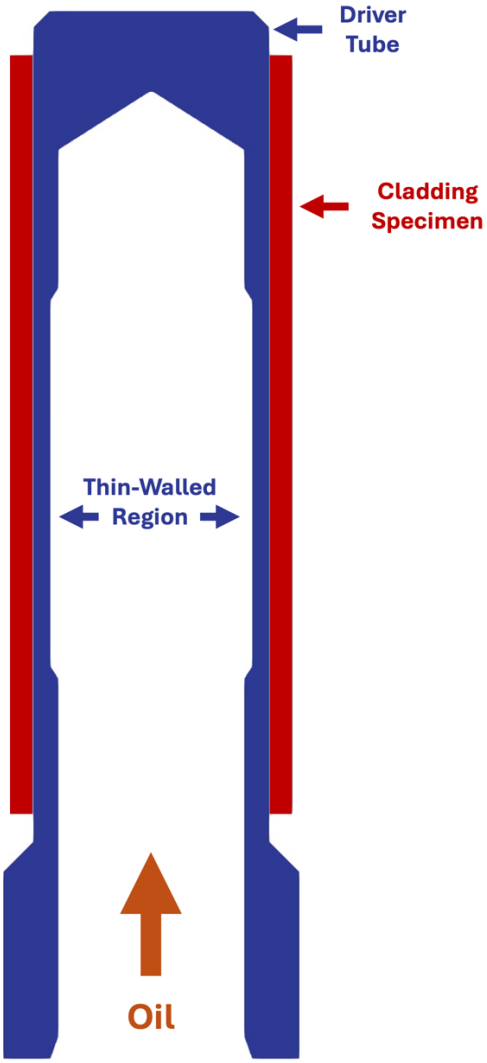

Figure 1. Schematic of driver tube and cladding assembly cross-section.

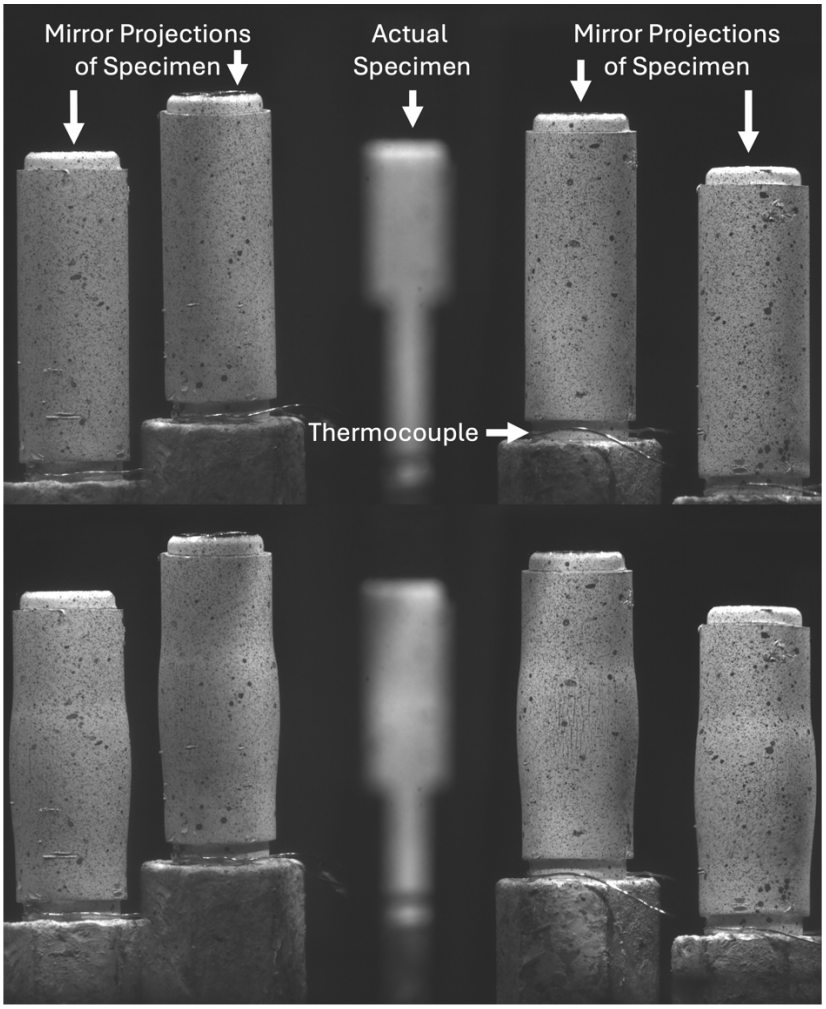

Figure 2. Images taken with telecentric lens and high-speed camera during a test. The top image was taken the moment pressurization started, and the bottom image was taken immediately before burst.

2.2 Experiment

Prepared specimens were attached to a nut via threads on the driver tube. The nut was then attached to an outlet nozzle on a hydraulic press. To experimentally simulate the effects of PCMI on the cladding, viscous hydraulic oil was rapidly injected through the nozzle into the driver tube. This treatment caused the thin-walled region of the driver tube to expand and apply a force to the cladding. Pressurization rates were determined by the velocity of a strike pin that initiated injection. Strike pin velocities ranged from 25.4 mm/s to 762 mm/s. Six first-surface mirrors and four ceramic heating elements were positioned around the specimen. The heating elements allowed for the execution of tests with the cladding at around 300 °C, which was confirmed by a K-type thermocouple wrapped around the bottom of the driver tube (see Figure 2). The mirrors projected four depictions of different sides of the specimen toward a single camera with a telecentric lens. This approach allowed for the DIC analysis of the entire specimen without introducing timing errors between multiple cameras. See Figure 3 for a detailed depiction of the test setup.

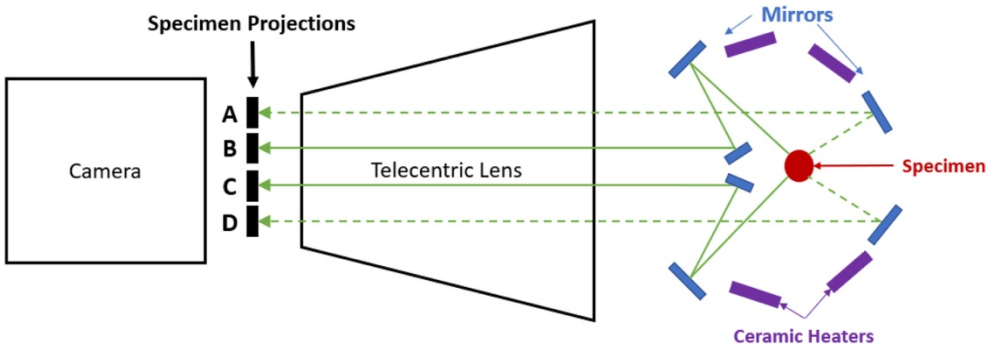

Figure 3. MBT setup schematic [22].

After painted specimens were attached to the outlet nozzle on the hydraulic press, the thermocouple was carefully hooked around the bottom of the specimen. Next, a custom quartz tank was placed over the setup. The quartz tank helped to contain the heat from the ceramic heaters to keep the specimen at the experimental temperature. Additionally, the quartz prevented the oil from spraying on the camera lens when burst occurred. The camera was focused, and lights were adjusted. Insulation was then placed over the quartz tank on all sides, and the ceramic heating elements were turned on. The temperature of the thermocouple was monitored until it reached 275 °C. In a previous study, it was found that when the bottom of the specimen—where the thermocouple contacts the cladding—is 275 °C, the center of the cladding is 300 °C [29]. The primary deformation occurs in the center of the cladding, making it essential that this location on the cladding be at an HZP-like temperature. Once the sample reached the proper temperature, the insulation was carefully removed from the quartz tank, and the test was performed. A pressure transducer recorded the pressure during the test while the camera captured images of the deforming specimen at frame rates in the range of 2000–10000 frames per second.

2.3 DIC Analysis

DIC is an analysis technique that allows the user to compute displacement values across the surface of a deforming specimen without any physical measurement instruments in contact with the specimen. DIC software does this by dividing an image into a grid of *subsets*, each of which is defined by the grayscale values it contains for each pixel. The matrix of grayscale values from an image of the deformed specimen is then compared to the matrices from an image of the undeformed specimen, the *reference image*, to track the movement of subsets through the deformation [30]. The resulting data is a series of displacement values across the specimen for each deformed image. This data can then be used to calculate values like strain. The spray-painted random speckle pattern applied to each specimen before testing provided the DIC software with distinct grayscale patterns to track during analysis. The speckle pattern must remain adhered to the specimen and deform with it, which is why tests were rapidly run after application while the paint was still malleable.

DIC engine (DICe), a software developed and maintained by Sandia National Laboratories, was utilized to analyze these tests [31–33]. Key details are outlined herein, but the reader is

directed to the work by Espersen et al. [34] for more information on the analysis process used in the present study. The subset-based full-field mode was used to analyze the entire surface of the cladding. Translation, normal stretch, and shear stretch shape functions were applied to each analysis. These shape functions helped DICe to process how the specimens were expected to deform between images. DIC software utilizes a *virtual strain gauge,* analogous to the area that a physical strain gauge foil covers, to compute the strain across the specimen [35]. Strain was computed with the default virtual strain gauge size, which is dependent on step size [31]. Subset size and step size, both measured in pixels, are two of the most important parameters in any DIC analysis. The subset size determines the area of the square that a DIC software uses to match pieces of subsequent images. For a subset size of 15 pixels, the software uses 15 × 15 pixel squares for matching. Larger subset sizes improve the quality of the software's matching by allowing it to compare more distinct features between images. However, when subsets are too large, the spatial resolution of calculated displacement values is lost [36]. A subset should, therefore, be small enough that the displacement gradient within it is nearly constant [30]. A DIC best practice is to select subset sizes so that one subset contains at least three distinct pattern features [35]. A technique developed in a previous study was utilized to determine subset sizes for these tests; in the selected technique, subset sizes are selected based on the relative fraction of light features on the specimen surface [34]. The fraction of light features represents the relative density of the speckle pattern on the specimen, which is one indication of speckle pattern quality. The step size, which is the distance between subsets, was chosen to be 1/3 of the subset size [35]. The regions of interest chosen for analysis were the entire areas of the cladding visible to the camera (see Figure 4). The analysis's resulting data was a comma-separated file (CSV) file for each image analyzed. Each CSV contained the DIC-calculated XX-, YY-, and XY-strain values at each subset. Because the straining to the cladding occurred mostly in the thin-walled region of the driver tube, the hoop strain at this location was most important for analysis. A Python post-processing script was used to sort the strain data into axial bins. To estimate the hoop strain, the XX-strain values at the axial location of the burst were averaged. This step also helped to decrease the effects of random errors in any one DIC strain calculation.

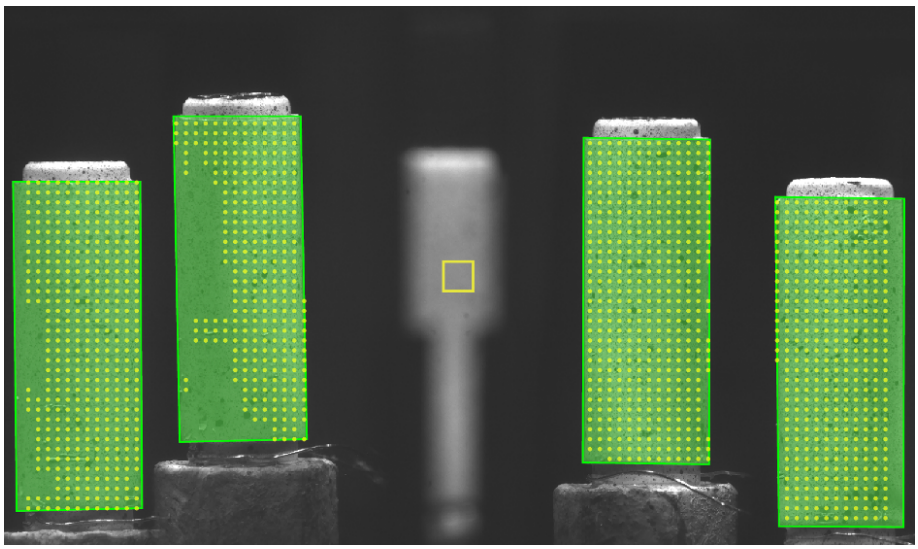

Figure 4. Regions of interest (highlighted in neon green) analyzed by the DIC software. The yellow square in the center is the size of a single subset for this test (33 pixels). The yellow dots on the regions of interest are the data points analyzed by DIC.

3. Results

3.1 Mechanical Test Results

As a case study, Figure 5 depicts the averaged in situ DIC hoop strain in the burst region for one of each material tested in addition to the respective applied pressures. The pressures are shown as solid lines and correspond with the right-hand y-axis. The hoop strain data points are represented by individual markers and are plotted on the left-hand y-axis. Based on a previous study, the error in DICe-calculated strain values is expected to be no more than 0.2% [34]. Error bars are not depicted in Figure 5 because they would be too small compared to the plot markers. Although the pressurizations for these three tests are not the same, they are within about 10 MPa of each other, allowing us to compare these three results. The cold spray-coated tube burst the earliest and at the lowest hoop strain of 10.0%. The PVD tube burst at a slightly lower hoop strain than the uncoated tube. These tubes burst at 11.5% and 11.9%, respectively. This case study indicates that the coated specimens may burst at lower hoop strains than the uncoated specimens, with the cold spray–coated tubes bursting at a significantly lower hoop strain than the other two tubes. This is investigated further by looking at the test results for all cases.

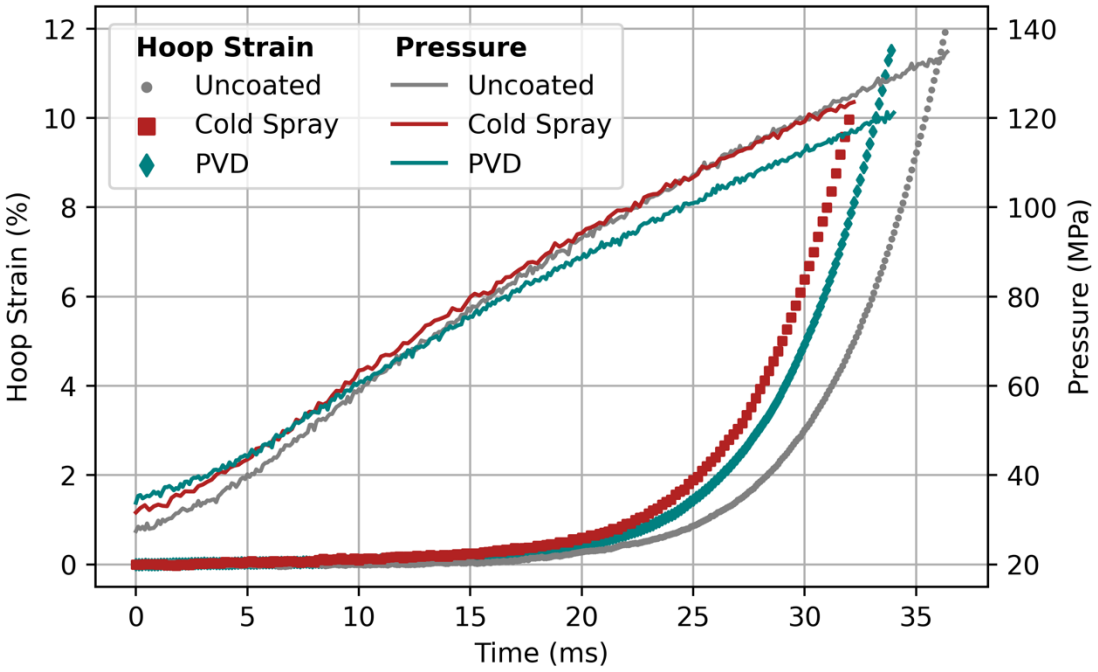

Figure 5. In situ hoop strain and pressure data for the 36.4 ms uncoated Zircaloy-4 test, the 32.2 ms cold spray–coated Zircaloy-4 test, and the 34 ms physical vapor deposition (PVD)–coated Zircaloy-4 test.

A summary of the results is given in Table 2, where the coating is specified in the left column. The pressure rise time indicates the amount of time from when pressurization was initiated to the point at which burst occurred. All specimens investigated in this study burst during testing. The average pressure rate was found by fitting a linear regression to the pressure data. The maximum pressure is the highest-pressure value recorded by the pressure transducer during the test. This was typically the value recorded immediately before burst. The failure hoop strain is the hoop strain measured with DIC immediately before burst. Finally, the minimum, maximum, and average hoop strain rates are reported. Pressure rise time and average pressure rate are inversely related, as expected. The maximum pressure held by the tube also appears to be inversely related to the average pressurization rate and directly related to the pressure rise time. This finding indicates that given a slower transient, the cladding can hold a larger amount of pressure. Additionally, the hoop strain rate is directly related to the average pressure rate, as expected. In general, faster pressurizations (shorter pressure rise times and higher pressurization rates) tend to result in lower maximum pressures and higher hoop strain rates.

Table 2. Results from MBTs.

Coating	Pressure Rise Time (ms)	Average Pressure Rate (GPa/s)	Maximum Pressure (MPa)	Failure Hoop Strain (%)	Minimum Hoop Strain Rate (%/s)	Maximum Hoop Strain Rate (%/s)	Average Hoop Strain Rate (%/s)
None	29.6	2.6542	120.48	8.8	1.4	2294	299.5
	36.4	3.0985	134.81	11.9	2.6	2259	328.5
	54.5	1.9352	139.2	10.8	0.36	2274	198.2
	57.8	1.5137	135.76	12.6	0.19	2094	218.2
	141.2	0.86115	149.3	17.2	0.055	895	121.7
	143.3	0.86819	159.74	11.7	0.20	1165	82.0
	778.0	0.23411	192.42	16.3	0.0026	207	21.0
Cold Sprayed	24.6	2.6412	99.13	11.0	3.3	3430	447.0
	32.2	3.0255	123.55	10.0	1.1	2115	311.4
	49.6	2.3037	127.11	7.3	0.20	1902	148.6
	145.0	1.0616	167.6	8.6	0.52	629	59.1
	652.6	0.23145	189.27	7.0	0.02	171	10.7
Physical Vapor Deposition	32.4	2.5799	116.12	9.1	0.88	2337	281.8
	34.0	2.6777	121.31	11.5	0.15	2438	339.8
	58.2	1.6553	133.56	9.4	0.011	1707	161.6
	142.5	0.83583	161.24	9.6	0.016	1110	67.5
	751.5	0.21667	197.18	10.0	0.0020	286	13.3

To visualize the positive correlation between the average pressurization rate and the maximum strain rate, these values were plotted together as shown in Figure 6, where each test is plotted with a distinct marker indicating the material used in the test. Additionally, a linear trendline was added for each material to show that the trend is generally consistent across all three tested materials. This correlation was also found in a previous MBT study [22]. These results confirm that a faster pressurization, analogous to a larger energy deposition during a RIA, results in a higher strain rate.

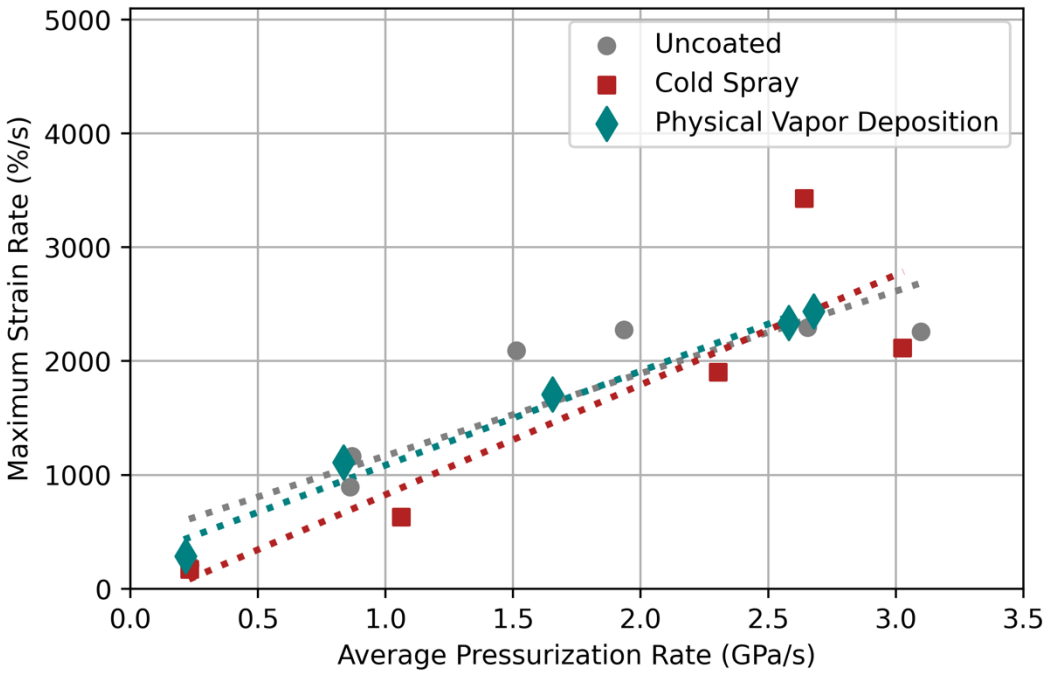

Figure 6. Maximum hoop strain rate vs. average pressurization rate. Linear fits of each material are included to show similar trends.

Next, the failure hoop strain was plotted against the maximum pressure held by the tube, as shown in Figure 7. The same symbols used in Figure 6 are used to depict each material, and trendlines are provided for each material. The uncoated Zircaloy-4 tests (gray circles) depict the trend we expected to see; with an increasing maximum pressure, the burst strain also increased. However, the PVD cases (teal diamonds) show that these tubes all burst with similar hoop strains independent of the maximum pressure in the tube. Finally, the cold spray–coated cases (red squares) show a negative correlation, implying that with increasing maximum pressure, the tubes burst with a lower hoop strain. More data is necessary to confirm these trends. However, the implication is that the coating caused the tubes to be more brittle than those in the uncoated control group. The two hypotheses proposed for this phenomenon are (1) the coating method resulted in the Zircaloy-4 becoming embrittled and (2) the coating is so well adhered to the surface of the cladding that when it cracks, the crack propagates into the Zircaloy, causing earlier burst. Hypothesis (1) would make the most sense for the cold spray samples, as cold spraying involves the bombardment of particles onto the surface of the Zircaloy. This may introduce dislocations in the lattice, causing it to lose ductility. Hypothesis (2) could hold true for either material, assuming that the adherence of the coating is strong enough.

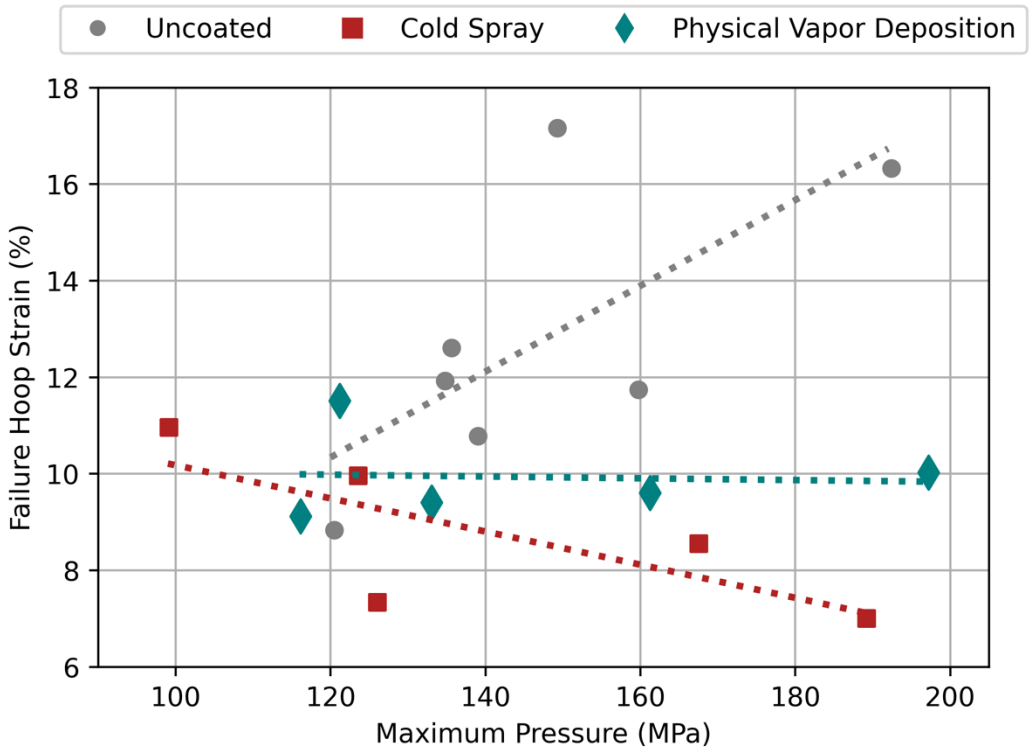

Figure 7. Hoop strain immediately before burst (failure hoop strain) vs. maximum pressure held by the tube. Linear trendlines are included for each material to depict trends.

3.2 Post Test Characterization

4. Conclusions

MBTs were performed on uncoated Zircaloy-4, cold spray–chromium-coated Zircaloy-4, and PVD–chromium-coated Zircaloy-4 tubes. These tests mimic the PCMI that occurs during the low-temperature phase of a RIA at HZP conditions. Hoop strains at burst were measured to be larger for the uncoated cases (8.8%–17.2%) than for the chromium-coated cases (7.0%–11.5%). Additionally, the cold spray–coated tubes burst at lower hoop strains (7.0%–11.0%) than the PVD tubes (9.1%–11.5%). While it is expected that the failure hoop strain increases with increasing maximum pressure, the PVD cases showed no correlation between those two values, and the cold-sprayed cases showed decreasing hoop strain with increasing maximum applied pressure. These results indicate that the chromium-coated Zircaloy-4 tubes are less ductile than the uncoated Zircaloy-4 tubes. To further understand the behaviors seen in these experiments, BISON modeling is being performed, and the results will be discussed in a future work.

5. Acknowledgements

This work was funded by a U.S. Department of Energy Nuclear Energy University Program Project (Grant: DE-NE0009212). This report was prepared as an account of work sponsored by an agency of the United States Government. Neither the United States Government nor any agency thereof, nor any of their employees, makes any warranty, express or implied, or assumes any legal liability or responsibility for the accuracy, completeness, or usefulness of any information, apparatus, product, or process disclosed, or represents that its use would not infringe privately owned rights. Reference herein to any specific commercial product, process, or service by trade name, trademark, manufacturer, or otherwise does not necessarily constitute or imply its endorsement, recommendation, or favoring by the United States Government or any agency thereof. The views and opinions of authors expressed herein do not necessarily state or reflect those of the United States Government or any agency thereof.

6. References

[1] K.A. Terrani, Accident tolerant fuel cladding development: Promise, status, and challenges, J. Nucl. Mater. 501 (2018) 13–30. https://doi.org/10.1016/j.jnucmat.2017.12.043.

[2] J.-D. Hong, H. Oh, D. Ahn, D. Jang, H.-G. Kim, J. Kim, H. Kim, M. Ševeček, Micro-mechanical evaluations of adhesion properties for Cr-coated accident tolerant fuel cladding, Nucl. Mater. Energy 41 (2024) 101799. https://doi.org/10.1016/j.nme.2024.101799.

[3] S.J. Zinkle, K.A. Terrani, J.C. Gehin, L.J. Ott, L.L. Snead, Accident tolerant fuels for LWRs: A perspective, J. Nucl. Mater. 448 (2014) 374–379. https://doi.org/10.1016/j.jnucmat.2013.12.005.

[4] J.-C. Brachet, T. Guilbert, S. Urvoy, E. Rouesne, M. Peyret, T. Vandenberghe, C. Prou, T. Le Hong, D. Hamon, Some practical methodologies to assess the overall high temperature (one-sided) steam oxidation protectiveness of chromium-based coatings on a zirconium-based substrate, as Enhanced – Accident tolerant (Nuclear) fuels (E-ATF) claddings, J. Nucl. Mater. 606 (2025) 155620. https://doi.org/10.1016/j.jnucmat.2025.155620.

[5] A. Tangirbergen, N. Amangeldi, S.T. Revankar, G. Yergaliuly, A review of irradiation-induced hardening in FeCrAl alloy systems for accident-tolerant fuel cladding, Nucl. Eng. Des. 429 (2024) 113659. https://doi.org/10.1016/j.nucengdes.2024.113659.

[6] J. Yang, H. Zhang, L. Yang, Y. Liu, J. Wang, X. He, L. Shang, J. Liao, D. Yun, S. Wang, D. Xu, Early-stage diffusion behavior of Cr-MEA coated Zr alloy accident tolerant fuel cladding materials at high temperature, Surf. Coat. Technol. 499 (2025) 131862. https://doi.org/10.1016/j.surfcoat.2025.131862.

[7] J. Ubaid, M. Alaleeli, S.A. Alameri, A. Schiffer, Thermomechanical analysis of SiC-based duplex claddings with varying thickness ratio for accident-tolerant nuclear fuel systems, Energy Convers. Manag. X 23 (2024) 100672. https://doi.org/10.1016/j.ecmx.2024.100672.

[8] S. Liu, Y. Wang, M. Deng, C. Liu, J. Liang, J. Yi, W. Xiao, Mechanical properties and high temperature structure evolution of FeCrAlMoNb high entropy alloy coatings with different Mo contents for accident tolerant fuel cladding, Intermetallics 179 (2025) 108670. https://doi.org/10.1016/j.intermet.2025.108670.

[9] J.W. Park, D. Ko, H. Jang, H. Kim, J. Lee, W. Choi, Algorithm for estimating Cr coating thickness for accident tolerant fuel cladding using a pancake ECT sensor, Nucl. Eng. Technol. 57 (2025) 103216. https://doi.org/10.1016/j.net.2024.09.019.

[10] F. Khoshahval, Neutron-physical characteristics of UO2 and UN/U3Si2 fuels with Zr, SiC and APMT accident tolerant claddings, Radiat. Phys. Chem. 222 (2024) 111869. https://doi.org/10.1016/j.radphyschem.2024.111869.
[11] W. Wang, G. Zhang, C. Wang, T. Wang, Y. Zhang, T. Xin, Insights into 1200 °C steam oxidation behavior of Cr coatings with different microstructure on Zircaloy-4 alloys for enhanced accident tolerant fuel cladding, Ann. Nucl. Energy 210 (2025) 110885. https://doi.org/10.1016/j.anucene.2024.110885.
[12] J. Yang, L. Shang, F. Zhao, K. Zinkovskii, X. He, Y. Cui, S. Wang, D. Yun, D. Xu, Early-stage diffusion and oxidation behavior of Cr-Nb coated Zr alloy accident tolerant fuel cladding materials at 1200°C–1500°C, J. Nucl. Mater. 599 (2024) 155257. https://doi.org/10.1016/j.jnucmat.2024.155257.
[13] J. Kim, C.Y. Lee, H. Rho, D. Kim, J. Lee, H. Jang, Y. Lee, Elucidating changes in thermal creep strain rate of Cr-coated Zr-Nb alloy Accident Tolerant Fuel (ATF) cladding via experiment and mechanical analysis, J. Nucl. Mater. 592 (2024) 154947. https://doi.org/10.1016/j.jnucmat.2024.154947.
[14] C.R.F. Azevedo, Selection of fuel cladding material for nuclear fission reactors, Eng. Fail. Anal. 18 (2011) 1943–1962. https://doi.org/10.1016/j.engfailanal.2011.06.010.
[15] I. Greenquist, A. Wysocki, J. Hirschhorn, N. Capps, Multiphysics analysis of fuel fragmentation, relocation, and dispersal susceptibility–Part 1: Overview and code coupling strategies, Ann. Nucl. Energy 191 (2023) 109913. https://doi.org/10.1016/j.anucene.2023.109913.
[16] A. Garde, G. Smith, R. Pirek, Effects of Hydride Precipitate Localization and Neutron Fluence on the Ductility of Irradiated Zircaloy-4, in: Zircon. Nucl. Ind. Elev. Int. Symp., ASTM International100 Barr Harbor Drive, PO Box C700, West Conshohocken, PA 19428-2959, 1996: pp. 407–430. https://doi.org/10.1520/STP16183S.
[17] H. Shah, J. Romero, P. Xu, B. Maier, G. Johnson, J. Walters, T. Dabney, K. Sridharan, Development of Surface Coatings for Enhanced Accident Tolerant Fuel (ATF), (2017).
[18] H.-G. Kim, I.-H. Kim, Y.-I. Jung, D.-J. Park, J.-Y. Park, Y.-H. Koo, Adhesion property and high-temperature oxidation behavior of Cr-coated Zircaloy-4 cladding tube prepared by 3D laser coating, J. Nucl. Mater. 465 (2015) 531–539. https://doi.org/10.1016/j.jnucmat.2015.06.030.
[19] M.N. Cinbiz, N.R. Brown, K.A. Terrani, R.R. Lowden, D. Erdman, A pulse-controlled modified-burst test instrument for accident-tolerant fuel cladding, Ann. Nucl. Energy 109 (2017) 396–404. https://doi.org/10.1016/j.anucene.2017.05.058.
[20] J. Ko, J.W. Kim, H.W. Min, Y. Kim, Y.S. Yoon, Review of manufacturing technologies for coated accident tolerant fuel cladding, J. Nucl. Mater. 561 (2022) 153562. https://doi.org/10.1016/j.jnucmat.2022.153562.
[21] K.O. Ott, R.J. Neuhold, Introductory Nuclear Reactor Dynamics, American Nuclear Society, 1985.
[22] N.R. Brown, B.E. Garrison, R.R. Lowden, M.N. Cinbiz, K.D. Linton, Mechanical failure of fresh nuclear grade iron–chromium–aluminum (FeCrAl) cladding under simulated hot zero power reactivity initiated accident conditions, J. Nucl. Mater. 539 (2020) 152352. https://doi.org/10.1016/j.jnucmat.2020.152352.
[23] M.N. Cinbiz, M. Gussev, K. Linton, K.A. Terrani, An advanced experimental design for modified burst testing of nuclear fuel cladding materials during transient loading, Ann. Nucl. Energy 127 (2019) 30–38. https://doi.org/10.1016/j.anucene.2018.11.051.

[24] K. Yueh, J. Karlsson, J. Stjärnsäter, D. Schrire, G. Ledergerber, C. Munoz-Reja, L. Hallstadius, Fuel cladding behavior under rapid loading conditions, J. Nucl. Mater. 469 (2016) 177–186. https://doi.org/10.1016/j.jnucmat.2015.11.032.
[25] K. Yueh, Applicability of modified burst test data to reactivity initiated accident, J. Nucl. Mater. 488 (2017) 338–345. https://doi.org/10.1016/j.jnucmat.2017.02.011.
[26] J.I. Espersen, B.E. Garrison, K. Linton, K. Shirvan, N.R. Brown, Preliminary Analysis of Reactivity Initiated Accident Separate Effects Mechanical Tests on Chromium-Coated Zirconium Cladding, in: Trans. Am. Nucl. Soc., Indianapolis, IN, 2023: pp. 290–292. https://doi.org/10.13182/T128-42108.
[27] J. Hazan, A. Gauthier, E. Pouillier, K. Shirvan, Semi-integral LOCA test of cold-spray chromium coated zircaloy-4 accident tolerant fuel cladding, J. Nucl. Mater. 550 (2021) 152940. https://doi.org/10.1016/j.jnucmat.2021.152940.
[28] Armeco, High Temperature Ceramic Adhesives, (2020). https://aremco.com/wp-content/uploads/2020/07/A02_S1_20.pdf.
[29] S.K. Lee, B.E. Garrison, N.A. Capps, G. Pastore, C.P. Massey, K.D. Linton, N.R. Brown, BISON validation of FeCrAl cladding mechanical failure during simulated reactivity-initiated accident conditions, J. Nucl. Mater. 564 (2022) 153676. https://doi.org/10.1016/j.jnucmat.2022.153676.
[30] M.A. Sutton, S.R. McNeill, J.D. Helm, Y.J. Chao, Advances in Two-Dimensional and Three-Dimensional Computer Vision, in: P.K. Rastogi (Ed.), Photomechanics, Springer, Berlin, Heidelberg, 2000: pp. 323–372. https://doi.org/10.1007/3-540-48800-6_10.
[31] D. Turner, An Overview of the Virtual Strain Gauge Formulation in DICe, Sandia National Laboratories (SNL), Albuquerque, NM, and Livermore, CA (United States), 2018. https://doi.org/10.2172/1528762.
[32] D. Turner, An Overview of the Gradient-Based Local DIC Formulation for Motion Estimation in DICe, Sandia National Laboratories (SNL), Albuquerque, NM, and Livermore, CA (United States), 2019. https://doi.org/10.2172/1561808.
[33] D. Turner, P. Reu, P. Crozier, Evaluation of various interpolants available in DICE, Sandia National Laboratories (SNL), Albuquerque, NM, and Livermore, CA (United States), 2015. https://doi.org/10.2172/1170515.
[34] J.I. Espersen, M.N. Cinbiz, N.A. Capps, N.R. Brown, A standardized analysis process using digital image correlation to calculate in-situ cladding strain from modified burst tests for fuel performance code validation, Nuclear Science and Engineering (Submitted for review).
[35] International Digital Image Correlation Society, E. Jones, M. Iadicola, R. Bigger, B. Blaysat, C. Boo, M. Grewer, J. Hu, A. Jones, M. Klein, K. Raghavan, P. Reu, T. Schmidt, T. Siebert, M. Simenson, D. Turner, A. Vieira, T. Weikert, A Good Practices Guide for Digital Image Correlation, 1st ed., International Digital Image Correlation Society, 2018. https://doi.org/10.32720/idics/gpg.ed1.
[36] B. Pan, H. Xie, Z. Wang, K. Qian, Z. Wang, Study on subset size selection in digital image correlation for speckle patterns, Opt. Express 16 (2008) 7037–7048. https://doi.org/10.1364/oe.16.007037.